Materials Horizons

ROYAL SOCIETY OF CHEMISTRY

CORRECTION

View Article Online
View Journal

Cite this: DOI: 10.1039/d3mh90012f

Correction: Tuning the arrangement of lamellar nanostructures: achieving the dual function of physically killing bacteria and promoting osteogenesis

Shi Mo,[ab] Kaiwei Tang,[bc] Qing Liao,[a] Lingxia Xie,[a] Yuzheng Wu,[b] Guomin Wang,[b] Qingdong Ruan,[b] Ang Gao,[a] Yuanliang Lv,[ad] Kaiyong Cai,[e] Liping Tong,*[a] Zhengwei Wu,*[bf] Paul K Chu[b] and Huaiyu Wang*[a]

DOI: 10.1039/d3mh90012f

rsc.li/materials-horizons

Correction for 'Tuning the arrangement of lamellar nanostructures: achieving the dual function of physically killing bacteria and promoting osteogenesis' by Shi Mo *et al.*, *Mater. Horiz.*, 2023, **10**, 881–888, https://doi.org/10.1039/d2mh01147f.

The authors regret that the address of Liping Tong in the published article was incorrectly given as "[b]Department of Physics, Department of Materials Science and Engineering, and Department of Biomedical Engineering, City University of Hong Kong, Tat Chee Avenue, Kowloon, Hong Kong, China"; it should be "[a]Institute of Biomedicine and Biotechnology, Shenzhen Institute of Advanced Technology, Chinese Academy of Sciences, Shenzhen, China". In addition, Liping Tong, Zhengwei Wu and Huaiyu Wang should all be marked with the asterisk symbol * to indicate that they are corresponding authors. The corrected author details are as shown herein.

The Royal Society of Chemistry apologises for these errors and any consequent inconvenience to authors and readers.

[a] *Institute of Biomedicine and Biotechnology, Shenzhen Institute of Advanced Technology, Chinese Academy of Sciences, Shenzhen, China. E-mail: lp.tong@siat.ac.cn, hy.wang1@siat.ac.cn*

[b] *Department of Physics, Department of Materials Science and Engineering, and Department of Biomedical Engineering, City University of Hong Kong, Tat Chee Avenue, Kowloon, Hong Kong, China*

[c] *School of Materials Science and Engineering, Xiangtan University, Xiangtan, China*

[d] *School of Advanced Manufacturing, Fuzhou University, Fuzhou, China*

[e] *Key Laboratory of Biorheological Science and Technology, Ministry of Education, College of Bioengineering, Chongqing University, Chongqing, China*

[f] *School of Nuclear Science and Technology, University of Science and Technology of China, Hefei, China. E-mail: wuzw@ustc.edu.cn*

Materials Horizons

ROYAL SOCIETY OF CHEMISTRY

COMMUNICATION

View Article Online
View Journal | View Issue

Cite this: *Mater. Horiz.*, 2023, 10, 881

Received 16th September 2022,
Accepted 6th December 2022

DOI: 10.1039/d2mh01147f

rsc.li/materials-horizons

Tuning the arrangement of lamellar nanostructures: achieving the dual function of physically killing bacteria and promoting osteogenesis†

Shi Mo,‡[ab] Kaiwei Tang,‡[bc] Qing Liao,[a] Lingxia Xie,[a] Yuzheng Wu,[b] Guomin Wang,[b] Qingdong Ruan,[b] Ang Gao,[a] Yuanliang Lv,[ad] Kaiyong Cai,[e] Liping Tong,[b] Zhengwei Wu,[bf] Paul K Chu[b] and Huaiyu Wang[a]

Bacteria killing behavior based on physical effects is preferred for biomedical implants because of the negligible associated side effects. However, our current understanding of the antibacterial activity of nanostructures remains limited and, in practice, nanoarchitectures that are created on orthopedics should also promote osteogenesis simultaneously. In this study, tilted and vertical nanolamellar structures are fabricated on semi-crystalline polyether-ether-ketone (PEEK) *via* argon plasma treatment with or without pre-annealing. The two types of nanolamellae can physically kill the bacteria that come into contact with them, but the antibacterial mechanisms between the two are different. Specifically, the sharp edges of the vertically aligned nanolamellae can penetrate and damage the bacterial membrane, whereas bacteria are stuck on the tilted nanostructures and are stretched, leading to eventual destruction. The tilted nanolamellae are more desirable than the vertically aligned ones from the perspective of peri-implant bone regeneration. Our study not only reveals the role of the arrangement of nanostructures in orthopedic applications but also provides new information about different mechanisms of physical antibacterial activity.

New concepts

Tuning the arrangement of nanolamellar structures for both bacterial eradication and bone regeneration is proposed, and the related mechanisms are discussed in detail. To investigate the biological effect of differently arranged nanolamellae, tilted and vertical nanolamellar structures are readily formed on PEEK implants, which yield physical antibacterial effects *via* different mechanisms. Different from the vertical nanolamellae, which kill bacteria through physical penetration of the bacterial membrane, the tilted nanostructures lead to bacterial stretching and deformation *via* strong interactions. Furthermore, the tilted nanolamellae perform better than the vertically aligned ones from the perspective of peri-implant osteogenesis. The concept proposed in this work offers a new strategy for designing nanostructures in the application of implantable biomaterials.

Introduction

Bacterial infections are one of the main challenges for clinical operations that involve open wounds, for which the common solution is postoperative antibiotic therapy.[1] However, the overuse of antibiotics has spurred the drug resistance of bacteria, consequently compromising their therapeutic effects and even leading to surgical failure.[2,3] Recently, antibiotic-free strategies have aroused interest in therapies against bacterial infection. For instance, the physical killing of pathogenic bacteria *via* photothermal treatment and electrical stimulation can circumvent the bacterial resistance caused by the overuse of antibiotics and can provide broad-spectrum antibacterial activity.[4–6] Nevertheless, these physical antibacterial strategies are only effective for the treatment of superficial bacterial infections within a limited tissue depth, but in many clinical operations, artificial prostheses are implanted deep inside the human body and are prone to postoperative bacterial infections. Hence, the development of new strategies to endow implants with the capability of physically killing bacteria is imperative.[7]

It is well recognized that incomplete disinfection of medical devices before surgery and the invasion of pathogenic bacteria

[a] *Institute of Biomedicine and Biotechnology, Shenzhen Institute of Advanced Technology, Chinese Academy of Sciences, Shenzhen, China. E-mail: lp.tong@siat.ac.cn, hy.wang1@siat.ac.cn*
[b] *Department of Physics, Department of Materials Science and Engineering, and Department of Biomedical Engineering, City University of Hong Kong, Tat Chee Avene, Kowloon, Hong Kong, China*
[c] *School of Materials Science and Engineering, Xiangtan University, Xiangtan, China*
[d] *School of Advanced Manufacturing, Fuzhou University, Fuzhou, China*
[e] *Key Laboratory of Biorheological Science and Technology, Ministry of Education, College of Bioengineering, Chongqing University, Chongqing, China*
[f] *School of Nuclear Science and Technology, University of Science and Technology of China, Hefei, China. E-mail: wuzw@ustc.edu.cn*

† Electronic supplementary information (ESI) available. See DOI: https://doi.org/10.1039/d2mh01147f

‡ Shi Mo and Kaiwei Tang contributed equally to this work.

into open wounds are the two primary reasons for the post-operative infection of long-term implants.[8] In both cases, although the number of pathogens reaching the artificial implants tends to be limited, a few of them can multiply rapidly if the surface conditions on the implants are favorable for bacterial colonization.[9] Hence, the construction of specific nanoarchitectures on surgical implants has been proposed to mitigate or eliminate bacterial infections.[10] This strategy is desirable as it can kill harmful germs that come into contact *via* physical interactions, without leading to drug resistance.[11] In particular, surface modification is an effective approach to optimize the biological, chemical, and physical properties of implants while preserving their favorable bulk mechanical properties. To this end, various nanostructures (nanorods, nanoknives, and so on) have been fabricated on implants made of titanium, magnesium, and other biomaterials to produce physical antibacterial characteristics.[10,12–14]

In general, most of the antibacterial nanostructures reported so far have sharp edges and/or burrs. At the microscopic level, the physical bactericidal effects hinge on interactions between the rigid nanostructures and elastic bacterial membranes. When the stretching force induced by the bacteria–material interaction is beyond the elastic limit of the bacterial membrane, irreversible physical damage, such as membrane rupture, can occur.[15,16] However, these effects are less obvious against Gram-positive bacteria, because there is a larger proportion of peptidoglycan in the cell wall of Gram-positive bacteria and the elasticity is greater than that of Gram-negative bacteria.[17] However, the sharp edges of nanostructures can have a detrimental impact on normal cells and can consequently compromise the healing of peri-implant tissue after surgery.[18] Therefore, these antibacterial nanostructures must be further optimized to foster proper tissue growth, and an antibacterial method that is different from direct piercing of the bacterial membrane is anticipated. Because bacteria are tiny and simple prokaryotes, and mammalian cells are larger eukaryotes with much more complicated systems, their modes of migration and propagation on solid surfaces are quite different, and this difference may enable the possibility of striking the delicate balance between the antibacterial activity needed and other properties that are required for bone-implant integration.[19,20]

With the deepening of research on bacterial behavior, there is an increasing awareness that the adhesion of bacteria onto solid surfaces is a multi-stage and sequential process that includes initial reversible adhesion and subsequent irreversible adhesion. Various physical effects such as van der Waals forces, Brownian motion, and electrostatic interactions are dominant during the initial reversible phase of bacterial adhesion,[21] whereas biomolecules such as adhesins and flagella and their interactions on the material surface play leading roles in the later irreversible stage. Moreover, the strength of the irreversible bacteria–material interactions that occur later is usually higher than that of the initial reversible bacterial adhesion.[22] This difference should be taken into account when developing techniques to modulate the antibacterial nanostructures on biomedical implants.

Herein, physical antibacterial effects are produced by constructing tilted nanolamellar structures on polyetheretherketone (PEEK), and a better osteogenic performance can be attained simultaneously to fulfill the multi-functional requirements of bone implantation materials. A simple and convenient technique of Ar plasma etching is combined with a pre-annealing treatment to tune the orientation of the constructed nanolamellae from vertical to tilted. This strategy is based on the semicrystalline structure of medical-grade PEEK in which the amorphous and crystalline phases are adjustable, resulting in different directional resistance to the Ar plasma. The antibacterial and osteogenic properties of the vertical and tilted nanolamellae are systematically studied both *in vitro* and *in vivo* and the antibacterial mechanisms are investigated. Different from the physical bactericidal effects of vertical nanolamellae *via* direct piercing of the bacterial membrane, the tilted nanolamellar structures can trap the attached bacteria through high affinity to quickly enter the stage of irreversible bacterial adhesion. As a consequence, the shearing force generated by bacterial motility competes with the strong adhesion force of the bacteria on the tilted nanolamellar structures, leading to serious deformation of the bacterial membrane and the eventual production of physical antibacterial effects.

Results and discussion

Formation of nanolamellae and characterization

As shown in Fig. 1a, the lamellar nanostructures are generated on PEEK through selective etching of the amorphous phase by the plasma (Fig. 1b) and the plasma parameters and crystalline phases of the substrate impact the formation of the nanolamellae. As the plasma processing time is increased to 45 minutes, tilted nanolamellae are formed gradually on the annealed PEEK substrate (denoted as P-TL) (Fig. S1, ESI†). However, under the same conditions, the nanostructures formed on PEEK without annealing are vertically aligned (denoted as P-VL). The scanning electron microscopy (SEM) image of P-VL shows that the thickness of the nanolamellae is 20–30 nm and the space between two nanolamellae is about 2–3 times the thickness (Fig. 1c). By contrast, the tilted nanolamellae on P-TL are less sharp, and the PEEK sample treated with the Ar plasma for only 5 minutes (denoted as Ar-5) shows a smoother surface. Side views of both the P-VL and P-TL samples were also obtained *via* SEM (Fig. S2, ESI†), from which the vertical or tilted orientation of the constructed nanolamellae is clearly shown.

Compared with using reactive O_2 or N_2 plasmas (Fig. S3, ESI†), which produce side effects such as chain scission and cross-linking in addition to etching of the polymer, unique lamellar structures are produced when using an Ar plasma since etching is the dominant process during this treament.[23,24] After Ar plasma treatment, the surface roughness and surface area are increased, as shown *via* atomic force microscopy (AFM, Fig. 1d–f). At the same time, the water contact angle measured on different samples is reduced from

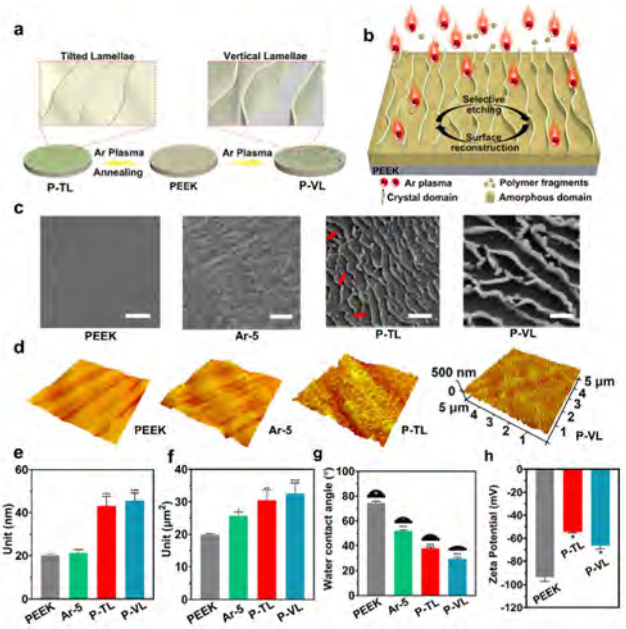

Fig. 1 Sample preparation and characterization. (a) Preparation of the different nanolamellae and representative structures. (b) Schematic illustrating the formation of lamellar nanostructures on PEEK. (c and d) SEM (c) and AFM (d) images of the different samples. The scale bar in (c) is 200 nm, and the red arrows indicate the nanolamellar structures in the P-TL sample. (e and f) Average roughness (e) and surface area (f) of the various samples. (g) Water contact angles of the different samples. (h) Zeta potentials of the different samples. * denotes $p < 0.05$, ** denotes $p < 0.01$ and *** denotes $p < 0.001$ compared with the PEEK group.

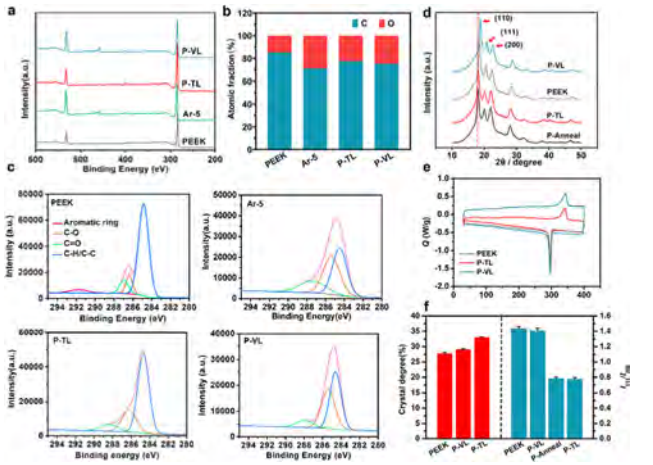

Fig. 2 Chemical and crystal properties of the different samples. (a) XPS survey spectra. (b) C and O concentrations. (c) High-resolution C 1s XPS spectra. (d) XRD spectra. (e) DSC curves. (f) Crystal degree determined *via* DSC and I_{111}/I_{200} determined using XRD.

74.3° for PEEK to 37.9° or 29.4° after the formation of vertical or tilted nanolamellae, respectively (Fig. 1g). The surface zeta potentials follow the order of P-TL > P-VL > PEEK (Fig. 1h).

To analyze the chemical composition and formation mechanism of the nanolamellae, X-ray photoelectron spectroscopy (XPS), attenuated total-reflectance Fourier transform infrared (ATR-FTIR) spectroscopy, and X-ray powder diffraction (XRD) were performed. As shown in Fig. 2a and b, only C and O are detected. The C concentration decreases from 85% to 75–77%, and that of O increases by about 10% after the plasma treatment. According to the high-resolution C 1s spectra, the peak originating from the $\pi \rightarrow \pi^*$ interaction almost disappears from the modified samples (Fig. 2c) because of cracking of the aromatic rings and damage to the polymer chain.[25,26] The ATR-FTIR spectra show similar peaks (Fig. S4, ESI†) confirming that the chemical changes occur near the surface.

As mentioned earlier, the amorphous phase of PEEK is eroded more easily than the crystalline phase by the plasma. The XRD peaks at 18.8°, 20.8°, 22.8°, and 28.9° from the untreated PEEK sample are related to the (110), (111), (200), and (211) planes, respectively (Fig. 2d).[27] In the pre-annealing step, chain relaxation/movement and rearrangement/crystallization occur and so the XRD peak of PEEK at 18.8° shifts slightly to a smaller diffraction angle after annealing, indicating a larger interplanar spacing. However, the interplanar spacing diminishes after formation of the lamellar nanostructures. This phenomenon is associated with lattice distortion caused by annealing or plasma treatment.[28] The crystalline phases were also analyzed using differential scanning calorimetry (DSC). As shown in Fig. 2e and f, the crystallinity of P-VL and P-TL is 29.09% and 33.02%, respectively, which is larger than 27.74% for untreated PEEK. The 111/200 ratio (I_{111}/I_{200}) decreases from 1.438 to 0.776 after annealing, probably related to the preferentially oriented growth of the crystal and the change in the crystal morphology (Fig. 2f).[29] Both XRD and DSC verify the difference in crystal structures of the various samples.

Microbicidal activity of the lamellar nanostructures

The microbicidal activity determined *via* colony forming unit (CFU) counting shows that both P-VL and P-TL can sterilize over 90% of the seeded *Staphylococcus aureus* (*S. aureus*), and the antibacterial rate against *Escherichia coli* (*E. coli*) is even higher due to its thinner cell wall (Fig. 3a). The antimicrobial efficacy is confirmed by staining the viable bacteria with green fluorescence (Fig. 3b) and quantified through intracellular release from the bacteria (Fig. 3c). Compared with the PEEK substrate, significantly less viable bacteria are observed for the P-VL and P-TL samples with lamellar nanostructures, and the intracellular release that is related to breakage of the bacterial membrane increases.

Antibacterial mechanisms of the nanolamellae

The morphologies of bacteria cultured on the different samples were examined using SEM. As shown in Fig. 4a, both the *E. coli* and *S. aureus* cells on the planar PEEK sample maintained a normal morphology, indicating that the surface of the unmodified sample is friendly to bacteria. The morphology of the bacteria cultured on Ar-5 also does not change, reflecting the limited antibacterial activity of this sample treatment. By contrast, the bacteria on the P-VL and P-TL samples have different shapes. In particular, some of the *E. coli* on P-TL are stuck on

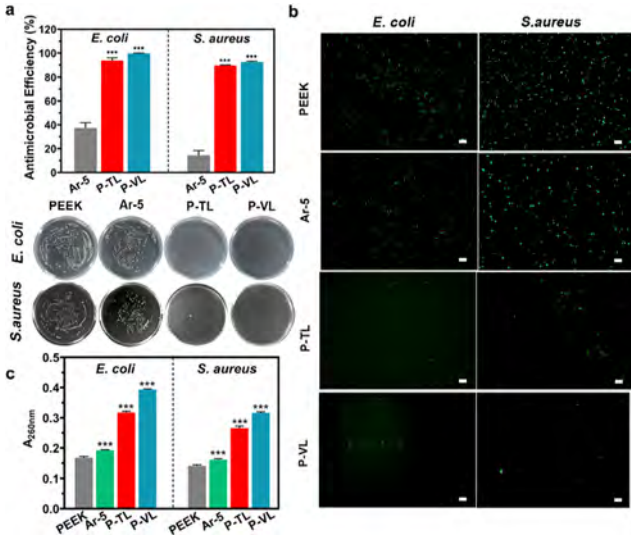

Fig. 3 *In vitro* antibacterial properties. (a) Antimicrobial efficiency and pictures of the bacterial colonies after different treatments. (b) Fluorescence images of the viable bacteria cultured on the different samples (scale bar = 20 μm). (c) Quantification of the intracellular substance released from the bacteria after different treatments. * denotes $p < 0.05$, ** denotes $p < 0.01$ and *** denotes $p < 0.001$ compared with the PEEK group.

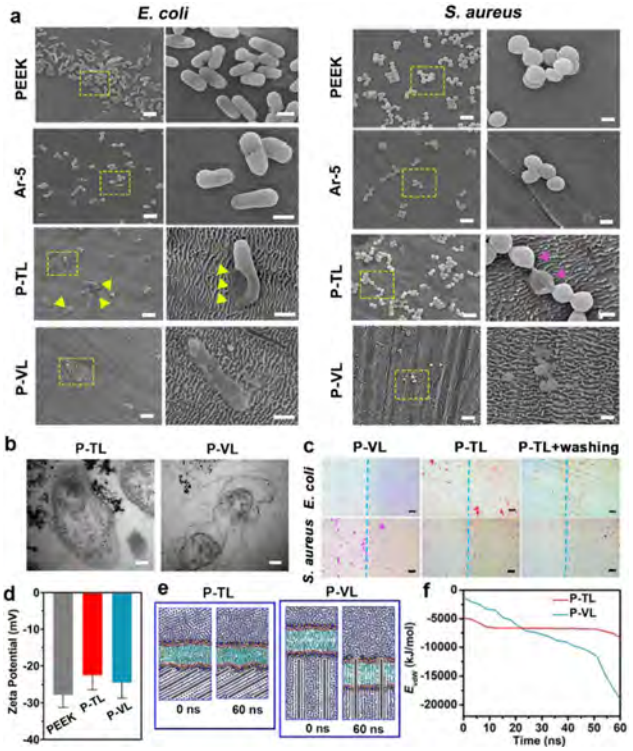

Fig. 4 Investigation of antibacterial mechanism. (a) SEM images of *E. coli* and *S. aureus* cultured on the different specimens, with the rightmost column of each showing enlarged versions of the marked area in the leftmost column. The yellow triangles indicate strong interactions between *E. coli* and P-TL, leading to bacterial swelling, and the magenta triangles show deformation of *S. aureus*. The scale bars are 2 μm (leftmost columns) and 500 nm (rightmost columns). (b) TEM images of *E. coli* cultured on P-TL and P-VL. The black points are the nanolamellae scraped from the samples. The scale bars are 100 nm. (c) Gram staining images for *E. coli* and *S. aureus* attached to partial P-VL and partial P-TL samples. The blue line represents the boundary between the PEEK region (left) and lamellar structures (right). The scale bars are 10 μm. (d) Zeta potentials for *E. coli* cultured on the different specimens. (e) Molecular dynamics simulations of the interactions between the PEEK nanoplates and the simulated bacterial membrane at 0 ns and 60 ns. (f) E_{vdw} between the bacterial membrane and the nanoplates, determined *via* simulation.

the obliquely aligned nanolamellae, leading to swelling and deformation (yellow arrows). A similar phenomenon can be observed for *S. aureus* on P-TL, albeit with less deformation (magenta arrows). This is because *S. aureus* has a round shape, a thicker cell wall, and a higher stiffness than *E. coli*.[17] Compared with P-TL, P-VL is more inhospitable for the bacteria as the vertically aligned nanolamellae destroy the bacterial membrane through physical penetration. The difference in the bacterial morphology was also observed using transmission electron microscopy (TEM, Fig. 4b). The bacteria on P-TL are swollen with partially indistinct membranes, and the strong interactions between the bacteria and the sample surface produce irreversible bacterial damage. By comparison, the physical damage observed for the bacteria on P-VL is more significant, as manifested by the severe deformation and rupture of the bacterial membrane as well as the leaked cytoplasm.

For a better understanding of the antibacterial mechanisms of the different nanolamellae, bacteria were cultured on samples partially constructed with the P-VL or P-TL nanostructures (Fig. S5, ESI†) and then visualized *via* Gram staining. As shown in Fig. 4c, nearly all the seeded bacteria prefer to adhere to the flat PEEK surface than the nanostructured P-VL. By comparison, the bacteria are distributed evenly in the flat and P-TL regions. Interestingly, most of the attached bacteria on the flat PEEK surface can be removed by washing, but those in the P-TL region can withstand the same washing, indicating that the adhesion force of the bacteria on the flat and P-TL regions is quite different.

To better understand the interactions between the bacteria and the different surface morphologies, the surface zeta potentials were measured after culturing *E. coli* on PEEK, P-TL, and P-VL for 6 hours. As shown in Fig. 4d, the surface potentials of *E. coli* harvested from P-TL and P-VL are −22.5 mV and −24.5 mV, respectively, which are less negative than that of the control (−27.8 mV). This is in line with previous reports that dead bacteria show a less negative zeta potential than living bacteria,[30,31] once again verifying the antibacterial effects of P-TL and P-VL.

Molecular dynamics simulations were also performed to assess the interactions between the bacteria and P-VL or P-TL. The results show that the vertically aligned nanolamellae can penetrate the cellular membrane of the bacteria upon contact, but the tilted nanolamellae do not cause direct penetration of the bacterial membrane (Fig. 4e). The van der Waals interaction (E_{vdw}) between the bacterial membrane and the vertically aligned nanolamellae increases gradually in the 60 ns dynamics simulation, but that of the tilted nanolamellae remains at about −5000 kJ mol^{-1} throughout the stimulation (Fig. 4f).

These results suggest that the strong interaction between the bacteria and the modified surface, rather than physical penetration of the bacterial membrane by the nanopattern, is responsible for the antimicrobial activity of P-TL with tilted nanolamellae.

In vitro osteogenetic evaluation

The adhesion and proliferation of osteoblasts occurs in the early stage of osteogenesis. Owing to the improved surface hydrophilicity and surface roughness, the plasma-treated PEEK facilitates cell growth in line with previous reports.[32,33]

Fig. 5a and b indeed show better adhesion and proliferation of osteoblasts on the modified samples. After culturing for 3 and 7 days, the cell viability shows the following order of Ar-5 > P-TL > P-VL > PEEK. Moreover, the osteoblasts on the modified surfaces are more stretched and show nuclei and a higher coverage (Fig. 5a). In individual cases, the morphology of the cells on P-VL is different from that on Ar-5 and P-TL. The magnified SEM images reveal that the vertically aligned nanolamellae with sharp edges have a strong impact on the morphology of some cultured cells, which are wrinkled and irregular in shape (Fig. S6, ESI†). By contrast, the tilted nanolamellar arrangement on P-TL imposes less stress on the attached cells and is thus more receptive to cell attachment and proliferation (Fig. 5b). This is in line with the results from the flow cytometry analysis of cells cultured on different samples, which show that the ratio of normal cells in the P-TL group is slightly higher than that determined for the PEEK and P-VL groups (Fig. S7, ESI†).

Osteogenic differentiation was further evaluated, where alkaline phosphatase (ALP) activity is one of the early biomarkers of osteogenesis.[34] As shown in Fig. 5c, the ALP activity on P-TL is higher than the other groups after osteogenic induction for 3 and 7 days. Besides the ALP activity, the mineralization of osteoblasts determined *via* alizarin red staining shows the highest level on P-TL (Fig. 5d and Fig. S8, ESI†). These are similar to the results of qPCR, showing that the levels of osteogenesis-related genes, including ALP, osteocalcin (OCN), and osteopontin (OPN), are highest on the P-TL sample after osteogenic induction for 14 and 21 days (Fig. 5e–g). Although osteogenic differentiation of the cells on P-VL is higher than that on the PEEK control, the outcome is not satisfactory because the ALP and OCN gene expression levels are lower than that on Ar-5. All in all, the *in vitro* results disclose that the nanomorphology of P-TL favors the adhesion and proliferation of osteoblasts and subsequently promotes osteogenic differentiation and mineralization.

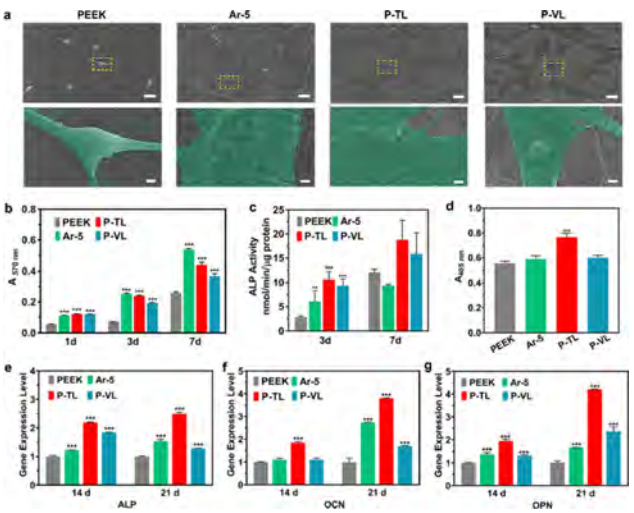

Fig. 5 *In vitro* characteristics of osteoblasts. (a) Morphology of osteoblasts cultured on the different samples for 1 day. The second row shows enlarged versions of the marked areas in the first row, with the cells shown as a pseudo-color. The scale bars are 20 μm (first row) and 2 μm (second row). (b) Viability of osteoblasts cultured on the different samples for 1, 3 and 7 days. (c) ALP activity of osteoblasts cultured on the different samples after osteogenic induction for 3 and 7 days. (d) Mineralization of osteoblasts cultured on the different samples after osteogenic induction for 14 days. (e–g) Osteogenic gene expression levels including (e) ALP, (f) OCN, and (g) OPN for osteoblasts cultured on the different samples after osteogenic induction for 14 and 21 days. * denotes $p < 0.05$, ** denotes $p < 0.01$ and *** denotes $p < 0.001$ compared with the PEEK group.

In vivo evaluation

The biological properties were evaluated *in vivo* by monitoring the antibacterial/anti-inflammatory response and osseointegration. First, the bacteria-contaminated samples were implanted subcutaneously into rats and, as shown in Fig. 6a and b, the fibrotic capsules elicited by the P-VL and P-TL implants were thinner than those surrounding the PEEK implant after 7 days, corroborating that the vertical and tilted nanolamellae are biocompatible and can even relieve the inflammatory response *in vivo* by eradicating peri-implant bacterial infection.[35]

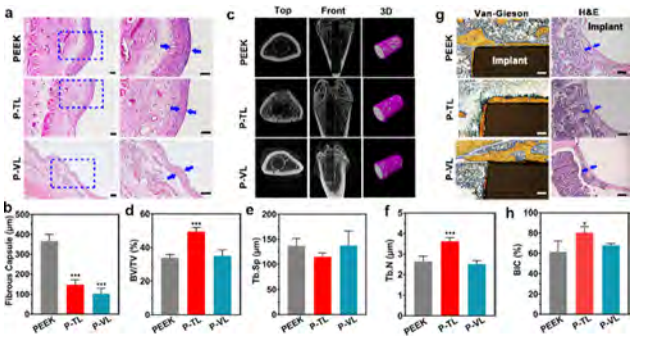

Fig. 6 *In vivo* antibacterial/anti-inflammatory characteristics and osseointegration. (a) H&E staining of the peri-implant tissues 7 days after subcutaneous implantation, with the fibrous layers marked by blue arrows. The right column shows enlarged versions of the marked areas in the left column. The scale bars are 200 μm. (b) Thickness of the fibrous layers in the different groups. (c) 2D and reconstructed 3D micro-CT images of the peri-implant tissues 8 weeks after bone implantation. (d–f) Quantitative micro-CT data for (d) BV/TV, (e) Tb.N, and (f) Tb.Sp. (g) Histological observation of the peri-implant tissues after Van Gieson and H&E staining, with the new bone marked by blue arrows. The scale bars are 200 μm. (h) BIC calculated from the histological images. * denotes $p < 0.05$, ** denotes $p < 0.01$ and *** denotes $p < 0.001$ compared with the PEEK group.

Furthermore, the samples were implanted into defects in the rat tibia and evaluated systematically 8 weeks after implantation. As shown in Fig. 6c, a large amount of new bone is formed surrounding the P-TL implant, but that surrounding the PEEK and P-VL implants is less dense. Bone regeneration based on the bone volume/total volume (BV/TV) and the trabecular number (Tb.N) is more substantial on P-TL with a relatively low trabecular separation (Tb.Sp), indicating that peri-implant bone remodeling of P-TL is better than that of PEEK and P-VL (Fig. 6d–f).[36] Osteointegration was further evaluated through Van Gieson and hematoxylin–eosin (H&E) staining. As shown in Fig. 6g, the bone layer in contact with the PEEK and P-VL implants is discontinuous and thin, but that on the P-TL implant is continuous and thick. According to the quantitative assessment, the percentage of bone-implant contact (BIC) for P-TL is 80.55%, which is high than 61.38% for PEEK and 68.19% for P-VL (Fig. 6h). Therefore, both the lamellar nanostructures and their tilted arrangement contribute to better osteogenesis on P-TL.

The surface morphology is an important factor in the design of biomedical implants, in order to satisfy the different requirements including bacterial resistance.[37–39] In this study, different nanolamellae were created on PEEK through annealing and Ar plasma treatment. In addition to the lamellar structure, treatment with reactive O_2 or N_2 plasma generates bumpy surfaces *via* etching as well as the combined effects of chain scission and surface functionalization (Fig. S3, ESI†). By contrast, treatment with Ar plasma mainly introduces physical etching effects for preferential ablation of the amorphous component in the polymer.[40,41] As a consequence, a zigzag lamellar structure can be formed. The role of the crystalline phases in the formation of the nanolamellae was analyzed by performing the same Ar plasma treatment on amorphous PEEK and polyphenylene sulfide (PPS). The modified surfaces are quite smooth without any obvious microstructures (Fig. S9, ESI†). Therefore, it can be inferred that the nanolamellae are generated *via* preferential etching of the amorphous domain in the semi-crystalline PEEK and surface reconstruction of the polymer components. The annealing pretreatment modifies the crystal structure of PEEK through preferentially oriented crystal growth, which is responsible for the formation of the different nanolamellae. These results show that the presence and arrangement of crystalline and amorphous phases in the semi-crystalline PEEK are both critical to the construction of different nanostructures *via* Ar etching.[42,43]

Pathogenic bacteria are invasive and can sense and adhere to favorable surfaces for unrestrained growth.[44] Unlike P-VL, which resists the adhesion of pathogenic bacteria, more *E. coli* attach to PEEK and P-TL with time, indicative of more 'bacteria-friendly' surfaces (Fig. S10, ESI†). Furthermore, different from the normal shape of bacteria on PEEK, some defects at the poles are observed from the bacteria on P-TL after incubation for only 1 and 3 hours (Fig. S11, ESI†), which can be ascribed to the strong interactions between the bacteria and the tilted nanolamellae (Fig. 4c). The *E. coli* cells cultured on the PEEK control and the P-TL sample have different diameters and lengths (Fig. S11 and S12, ESI†), further confirming that P-TL is detrimental to bacterial growth after attachment. In order to elucidate the possible antibacterial mechanism for P-TL, a short Ar plasma treatment (5 min) was performed, and the modified Ar-5 sample without lamellar nanotopography also showed a stronger bacterial affinity than PEEK, even after flushing (Fig. S13, ESI†). This is probably due to the highly negative surface zeta potential of PEEK (Fig. 1h), which leads to a weak interaction with the negatively charged bacteria. However, the antibacterial characteristics of Ar-5 are far from satisfactory (Fig. 3), meaning that the surface affinity and the lamellar nanotopography are both indispensable for bacterial killing on P-TL. It is possible that the attached *E. coli* cells try to migrate on the surface of P-TL in a run-and-tumble manner but are stuck on the nanostructures instead, leading to the stretching and rupture of the bacterial membranes.[45–47] As for *S. aureus*, the bacteria do not have pili or flagella and use another strategy called colony spreading for their motility.[48] Consequently, the swelling and deformation of *S. aureus* are not as obvious as for *E. coli* on the P-TL sample. With regard to the interactions between the bacteria and P-VL, it is easy to understand that the vertically aligned nanolamellae with sharp edges can kill the attached bacteria directly through piercing, as previously reported. However, with regard to P-TL, a totally different mechanism is proposed, for the first time, in which bacterial affinity and motility are involved in the physical antibacterial process of bacteria–material interactions.

Another key point is the different adaptability of osteoblasts and bacteria on surfaces with specific nanostructures. As demonstrated in our study, osteoblasts adapt better than bacteria on both P-TL and P-VL. This is because the cytoskeletons of prokaryotic and eukaryotic cells and their regulation mechanisms are different. The cytoskeleton of bacteria consists of filaments, which lack motor proteins and can only be driven *via* polymerization/depolymerization of the filaments. However, as for the eukaryotic cells, the cytoskeleton has a more complex and stable polymeric filamentous structure that includes actin based microfilaments, tublin based microtubules, intermediate filaments, and dynamic structures such as tubulin-derived microtubular structures and actin filaments, which can assemble, disassemble, and redistribute rapidly in the cells in response to subtle or drastic changes in the external environment.[49] Therefore, even when P-TL and P-VL samples are contaminated by bacteria, they can rapidly inactivate the bacteria in contact with them and enable cell growth thereafter (Fig. S14, ESI†). What is more, of the two kinds of sample that have a physical bacteria-killing capability, only P-TL can facilitate osteogenesis *in vitro* and *in vivo* because the tilted nanolamellae created on P-TL are not too inhospitable. A delicate balance between the antibacterial capability and osteogenesis required for bone-implant integration is thus attained. All in all, our work reveals a simple and effective strategy to produce multiple functions on PEEK that can fulfill the diverse and strict requirements of bone implantation, which is also inspirational pertaining to the surface functionalization of biomaterials in other disciplines.

Conclusions

Nanolamellar structures with different arrangements were constructed on PEEK, and their antibacterial and osteogenic properties were investigated systematically. The Ar plasma treatment can be used for nanolamellar construction by taking advantage of the different etching effects of the amorphous and crystalline phases, and the arrangement of the nanolamellae from being vertical to tilted is tailored through pre-annealing. Both the vertical and tilted nanolamellae show physical antibacterial effects but their mechanisms are totally different. The vertical nanolamellae with sharp edges puncture the bacterial membrane upon contact, whereas the tilted nanolamellae lead to bacterial inactivation on account of the strong interactions and stretching forces. In addition, the tilted nanolamellae create a favorable environment for the attachment, proliferation, and osteogenic differentiation of osteoblasts that consequently promotes integration of the bone implant. Our results provide a better understanding of the antibacterial mechanisms and osteogenic properties of different surface nanoarchitectures to aid the design and fabrication of advanced multifunctional biomaterials.

Author contributions

Conceptualization: S. Mo, K. Tang, H. Wang; methodology: S. Mo, K. Tang, Q. Liao, L. Xia, G. Wang, Q. Ruan, L. Tong; investigation: S. Mo, A. Gao, Y. Wu, H. Wang; supervision: H. Wang, L. Tong, P.K. Chu; writing – original draft: S. Mo; writing – review and editing: H, Wang, P.K. Chu, K. Cai. Z.W. Wu.

Conflicts of interest

There are no conflicts to declare.

Acknowledgements

The authors acknowledge financial support from the National Key Research and Development Program of China (2017YFA0701303 and 2021YFB3800800), the National Natural Science Foundation of China (31922040, 82172397 and 82272157), Shenzhen Science and Technology Research Funding (JCYJ20180507182637685, JCYJ20190806165616542, and JSGG20200225152648408), the Youth Innovation Promotion Association of the Chinese Academy of Sciences (No. 2020353), the China Postdoctoral Science Foundation (2021M693280), the Guangdong Basic and Applied Basic Research Foundation (No. 2020B1515120078), the City University of Hong Kong Donation Research Grant (DON-RMG 9229021), the City University of Hong Kong Donation Grant (9220061), the Hong Kong PDFS - RGC Postdoctoral Fellowship Scheme (PDFS2122-1S08 and CityU 9061014), as well as the Hong Kong HMRF (Health and Medical Research Fund) (2120972 and CityU 9211320). We acknowledge discussions with Yujun Feng, Hongyao Yin, and Gang Zhu from Sichuan University.

References

1 S. J. Baker, D. J. Payne, R. Rappuoli and E. De Gregorio, *Proc. Natl. Acad. Sci. U. S. A.*, 2018, **115**, 12887–12895.
2 N. J. Hickok and I. M. Shapiro, *Adv. Drug Delivery Rev.*, 2012, **64**, 1165–1176.
3 J. M. V. Makabenta, A. Nabawy, C.-H. Li, S. Schmidt-Malan, R. Patel and V. M. Rotello, *Nat. Rev. Microbiol.*, 2021, **19**, 23–36.
4 G. Qing, X. Zhao, N. Gong, J. Chen, X. Li, Y. Gan, Y. Wang, Z. Zhang, Y. Zhang, W. Guo, Y. Luo and X.-J. Liang, *Nat. Commun.*, 2019, **10**, 4336.
5 S. Liu, H. Yuan, H. Bai, P. Zhang, F. Lv, L. Liu, Z. Dai, J. Bao and S. Wang, *J. Am. Chem. Soc.*, 2018, **140**, 2284–2291.
6 C. Cao, W. Ge, J. Yin, D. Yang, W. Wang, X. Song, Y. Hu, J. Yin and X. Dong, *Small*, 2020, **16**, 2000436.
7 S. Rigo, C. Cai, G. Gunkel-Grabole, L. Maurizi, X. Zhang, J. Xu and C. G. Palivan, *Adv. Sci.*, 2018, **5**, 1700892.
8 C. T. Johnson, J. A. Wroe, R. Agarwal, K. E. Martin, R. E. Guldberg, R. M. Donlan, L. F. Westblade and A. J. García, *Proc. Natl. Acad. Sci. U. S. A.*, 2018, **115**, E4960–E4969.
9 R. J. Crawford, H. K. Webb, V. K. Truong, J. Hasan and E. P. Ivanova, *Adv. Colloid Interface Sci.*, 2012, **179–182**, 142–149.
10 D. P. Linklater, V. A. Baulin, S. Juodkazis, R. J. Crawford, P. Stoodley and E. P. Ivanova, *Nat. Rev. Microbiol.*, 2021, **19**, 8–22.
11 A. Tripathy, P. Sen, B. Su and W. H. Briscoe, *Adv. Colloid Interface Sci.*, 2017, **248**, 85–104.
12 M. Yang, S. Qiu, E. Coy, S. Li, K. Załęski, Y. Zhang, H. Pan and G. Wang, *Adv. Mater.*, 2022, **34**, 2106314.
13 D. Wang, F. Peng, J. Li, Y. Qiao, Q. Li and X. Liu, *Mater. Today*, 2017, **20**, 238–257.
14 G. Wang, W. Jiang, S. Mo, L. Xie, Q. Liao, L. Hu, Q. Ruan, K. Tang, B. Mehrjou, M. Liu, L. Tong, H. Wang, J. Zhuang, G. Wu and P. K. Chu, *Adv. Sci.*, 2020, **7**, 1902089.
15 J. Hasan, R. J. Crawford and E. P. Ivanova, *Trends Biotechnol.*, 2013, **31**, 295–304.
16 J. M. Sadowska, K. J. Genoud, D. J. Kelly and F. J. O'Brien, *Mater. Today*, 2021, **46**, 136–154.
17 S. Pogodin, J. Hasan, V. A. Baulin, H. K. Webb, V. K. Truong, T. H. Phong Nguyen, V. Boshkovikj, C. J. Fluke, G. S. Watson, J. A. Watson, R. J. Crawford and E. P. Ivanova, *Biophys. J.*, 2013, **104**, 835–840.
18 V. T. H. Pham, V. K. Truong, D. E. Mainwaring, Y. Guo, V. A. Baulin, M. Al Kobaisi, G. Gervinskas, S. Juodkazis, W. R. Zeng, P. P. Doran, R. J. Crawford and E. P. Ivanova, *J. Mater. Chem. B*, 2014, **2**, 2819–2826.
19 D. L. Bodor, W. Pönisch, R. G. Endres and E. K. Paluch, *Dev. Cell*, 2020, **52**, 550–562.
20 N. Wadhwa and H. C. Berg, *Nat. Rev. Microbiol.*, 2022, **20**, 161–173.
21 U. Filipović, R. G. Dahmane, S. Ghannouchi, A. Zore and K. Bohinc, *Adv. Colloid Interface Sci.*, 2020, **283**, 102228.
22 C. Berne, C. K. Ellison, A. Ducret and Y. V. Brun, *Nat. Rev. Microbiol.*, 2018, **16**, 616–627.

23 Z. A. Lewicka, A. Bahloul, W. W. Yu and V. L. Colvin, *Nanoscale*, 2013, **5**, 11071.
24 R. M. France and R. D. Short, *Langmuir*, 1998, **14**, 4827–4835.
25 S. Zhang, F. Awaja, N. James, D. R. McKenzie and A. J. Ruys, *Colloids Surf., A*, 2011, **374**, 88–95.
26 G. S. Oehrlein, R. J. Phaneuf and D. B. Graves, *J. Vac. Sci. Technol., B: Nanotechnol. Microelectron.: Mater., Process., Meas., Phenom.*, 2011, **29**, 010801.
27 A. M. Díez-Pascual and A. L. Díez-Vicente, *ACS Appl. Mater. Interfaces*, 2015, **7**, 5561–5573.
28 S. L. Weeks, A. Pal, V. K. Narasimhan, K. A. Littau and T. Chiang, *ACS Appl. Mater. Interfaces*, 2017, **9**, 13440–13447.
29 X. Sun, S. Dong and E. Wang, *Langmuir*, 2005, **21**, 4710–4712.
30 H. Lee, Y. Jin and S. Hong, *J. Photochem. Photobiol., B*, 2018, **185**, 136–142.
31 K. A. Soni, A. K. Balasubramanian, A. Beskok and S. D. Pillai, *Curr. Microbiol.*, 2008, **56**, 93–97.
32 L. Bacakova, E. Filova, M. Parizek, T. Ruml and V. Svorcik, *Biotechnol. Adv.*, 2011, **29**, 739–767.
33 A. H. C. Poulsson, D. Eglin, S. Zeiter, K. Camenisch, C. Sprecher, Y. Agarwal, D. Nehrbass, J. Wilson and R. G. Richards, *Biomaterials*, 2014, **35**, 3717–3728.
34 N. Li, L. Zhou, W. Xie, D. Zeng, D. Cai, H. Wang, C. Zhou, J. Wang and L. Li, *Chem. Eng. J.*, 2019, **371**, 618–630.
35 G. Wick, A. Backovic, E. Rabensteiner, N. Plank, C. Schwentner and R. Sgonc, *Trends Immunol.*, 2010, **31**, 110–119.
36 Z. Zhao, G. Li, H. Ruan, K. Chen, Z. Cai, G. Lu, R. Li, L. Deng, M. Cai and W. Cui, *ACS Nano*, 2021, **15**, 13041–13054.
37 Y. Luan, S. Liu, M. Pihl, H. C. van der Mei, J. Liu, F. Hizal, C.-H. Choi, H. Chen, Y. Ren and H. J. Busscher, *Curr. Opin. Colloid Interface Sci.*, 2018, **38**, 170–189.
38 S. G. Higgins, M. Becce, A. Belessiotis-Richards, H. Seong, J. E. Sero and M. M. Stevens, *Adv. Mater.*, 2020, **32**, 1903862.
39 D. Chopra, K. Gulati and S. Ivanovski, *Mater. Today Adv.*, 2021, **12**, 100176.
40 Z. K. Zander and M. L. Becker, *ACS Macro Lett.*, 2018, **7**, 16–25.
41 A. Dupuis, T. H. Ho, A. Fahs, A. Lafabrier, G. Louarn, J. Bacharouche, A. Airoudj, E. Aragon and J.-F. Chailan, *Appl. Surf. Sci.*, 2015, **357**, 1196–1204.
42 S. Himmelberger, J. Dacuña, J. Rivnay, L. H. Jimison, T. McCarthy-Ward, M. Heeney, I. McCulloch, M. F. Toney and A. Salleo, *Adv. Funct. Mater.*, 2013, **23**, 2091–2098.
43 J.-Z. Xu, Y.-Y. Liang, G.-J. Zhong, H.-L. Li, C. Chen, L.-B. Li and Z.-M. Li, *J. Phys. Chem. Lett.*, 2012, **3**, 530–535.
44 V. Carniello, B. W. Peterson, H. C. van der Mei and H. J. Busscher, *Adv. Colloid Interface Sci.*, 2018, **261**, 1–14.
45 M. J. Kühn, F. K. Schmidt, B. Eckhardt and K. M. Thormann, *Proc. Natl. Acad. Sci. U. S. A.*, 2017, **114**, 6340–6345.
46 M. Molaei, M. Barry, R. Stocker and J. Sheng, *Phys. Rev. Lett.*, 2014, **113**, 068103.
47 E. Perez Ipiña, S. Otte, R. Pontier-Bres, D. Czerucka and F. Peruani, *Nat. Phys.*, 2019, **15**, 610–615.
48 E. J. G. Pollitt and S. P. Diggle, *Cell. Mol. Life Sci.*, 2017, **74**, 2943–2958.
49 G. Jekely, *Cold Spring Harbor Perspect. Biol.*, 2014, **6**, a016030.

Electronic supplementary information

Tuning the arrangement of lamellar nanostructures: achieving dual functions of physical killing bacteria and promoting osteogenesis

Shi Mo, [ab] Kaiwei Tang, [bc] Qing Liao, [a] Lingxia Xie, [a] Yuzheng Wu, [b] Guomin Wang, [b] Qingdong Ruan, [b] Ang Gao, [a] Yuanliang Lv, [ad] Kaiyong Cai, [e] Liping Tong, *[a] Zhengwei Wu, *[bf] Paul K Chu, [b] Huaiyu Wang *[a]

[a] *Institute of Biomedicine and Biotechnology, Shenzhen Institute of Advanced Technology, Chinese Academy of Sciences, Shenzhen, China*

[b] *Department of Physics, Department of Materials Science and Engineering, and Department of Biomedical Engineering, City University of Hong Kong, Tat Chee Avene, Kowloon, Hong Kong, China*

[c] *School of Materials Science and Engineering, Xiangtan University, Xiangtan, China*

[d] *School of Advanced Manufacturing, Fuzhou University, Fuzhou, China*

[e] *Key Laboratory of Biorheological Science and Technology, Ministry of Education, College of Bioengineering, Chongqing University, Chongqing, China*

[f] *School of Nuclear Science and Technology, University of Science and Technology of China, Hefei, China*

* E-mail: lp.tong@siat.ac.cn (L. Tong); wuzw@ustc.edu.cn (Z. Wu); hy.wang1@siat.ac.cn (H. Wang).

Contents

A. Materials and methods

Preparation of the nanolamellar structures

To prepare the tilted structure, the medical grade and semi-crystalline PEEK plates (GEHR Plastics Hong Kong Ltd., China) with dimensions of Φ15 × 2 mm were annealed (10˚C min^{-1} to 180˚C) and cooled in an argon atmosphere (denoted as P-Anneal). No annealing was performed in the preparation of the vertically aligned lamellae. The annealed and un-annealed PEEK samples were polished with 2000 and 4000 grade silicon carbide papers, ultrasonically cleaned in 96% ethanol and pure water sequentially, and dried with flowing nitrogen. For fabricating P-VL and P-TL samples, the annealed and un-annealed PEEK were then subjected to an Ar plasma treatment for 45 minutes using the AJA International, Inc. system equipped with a radio frequency source at a pressure of 1.6×10^{-2} Torr. Afterwards, the samples were cleaned in a water bath ultrasonically and then dried with flowing nitrogen. For comparison, the semi-transparent and amorphous PEEK film (Goodfellow Corporation, UK) was treated under the same conditions. To prepare the partial P-VL and P-TL samples, two regions of the PEEK substrates were shielded by silicon wafers with only the middle region exposed to the plasma as shown in Figure S4.

Material characterization

The surface topography was examined by scanning electron microscopy (SEM, XL30 FEG, Philips, Netherlands) and atomic force microscopy (AFM, NanoScope V MultiMode, Veeco, USA). The static contact angles of water or diiodomethane (4 μL) were measured by the sessile drop method on a Rame'-Hart instrument (USA) under ambient conditions and the surface energy was determined accordingly. X-ray photoelectron spectroscopy (XPS, *K-Alpha*$^{+}$, Thermo Fisher Scientific, USA) with Al K_α excitation (72 W) and attenuated total-reflection Fourier transform infrared spectroscopy (ATR-FTIR, Frontier, PerkinElmer, USA) were employed to analyze the chemical structure. X-ray powder diffractometry (XRD, D2 Phaser, Bruker, Germany) was performed in the 2 theta range from 10^{o} to 50^{o} and 0.02^{o} per step and differential scanning calorimetry (DSC, 404 F3 Pegasus, Netzsch, Germany) was carried out from 30 to 400˚C at a heating rate of 10˚C/min. The crystalline degree was determined using the melting enthalpy ΔH_m of the samples and the ideal crystalline PEEK (130 J g^{-1}). The zeta potential was measured using 1 mM KCl solution with adjusted pH (0.05 M HCl/KOH) on an electrokinetic analyzer (Surpass3, Anton Paar, Austria).

In vitro antibacterial assays

Gram-positive *Staphylococcus aureus* (*S. aureus*) and Gram-negative *Escherichia coli* (*E. coli*) were obtained from the American Type Culture Collection (ATCC) and used in the antibacterial assays. Initially, the plate counting method was used to evaluate the antibacterial activity on the different samples. The bacteria were cultured in the Luria-Bertani (LB) medium in a shaker at 37 ˚C to reach an optical density at 600 nm (OD_{600}) = 0.1. After diluting 10^3 times with the sterilized physiological saline, 100 μL of each bacteria suspension was added to the sterilized samples on a 24-well plate (NEST Biotechnology, China) and cultured for different periods of time. Subsequently, 900 μL of the sterilized physiological saline were added to each well to elute the bacteria and 10 μL of the bacterial eluent were added to an agar plate and incubated at 37°C for 24 hours before colony forming unit (CFU) counting. The antimicrobial efficiency was evaluated according to the following equation:

$$\text{Antimicrobial efficiency} = \frac{CFU_{control} - CFU_{test}}{CFU_{control}} \times 100\%$$

Fluorescent staining was performed to visualize the viable bacteria on the different samples. 100 μL of the bacterial suspension (10^7 CFU mL^{-1}) were added to the samples, incubated for 6 hours, washed twice with the phosphate buffered saline (PBS, pH = 7.4), and stained by the Live/Dead Baclight bacterial viability kit (Thermo Fisher Scientific, USA) in the dark for 15 min. Afterwards, the unstained dye was rinsed with PBS three times and the viable bacteria were observed under an inverted fluorescent microscope (Axio Observer Z1, Zeiss, Germany). To assess the integrity of the bacterial membrane, the bacteria were detached from the different samples by ultrasonic elution. The detached bacteria were centrifuged at 5,000 revolutions per min (rpm) and the absorbance of the released cytoplasm in the supernatant was measured at 260 nm using an ultraviolet spectrophotometer (TU-1080PC, Persee, China).

Bacterial morphology

To analyze the morphological change on the bacteria, 100 μL of the bacterial suspension (10^7 CFU mL^{-1}) were added to the different samples and cultured for up to 6 hours. Afterwards, the samples with bacteria were rinsed thrice with PBS, immobilized with 4% glutaraldehyde solution, dehydrated with gradient ethanol, and dried at 37 ˚C prior to SEM observation. In addition, 100 μL of the bacteria media (10^9 CFU mL^{-1}) were cultured on the different samples for 6 hours, immobilized with 4% glutaraldehyde solution, and then harvested from the sample surface using a sterile surgical skin prep blade. The bacteria were immobilized again with 4%

osmium tetroxide, rinsed twice with PBS, dehydrated with gradient ethanol and acetone, embedded in epoxy resin, and sliced into thin sections. After uranyl acetate staining, the sections were loaded on a copper mesh and observed by transmission electron microscopy (TEM, H-7650, Hitachi, Japan).

Bacterial interactions with different nanolamellae

To determine bacterial chemotaxis and selective adhesion on the samples, the PEEK substrates partially modified (constructed with P-VL/P-TL nanolamellae or plasma-treated for 5 min) were cultured with *E. coli* and *S. aureus* for 6 hours, respectively. The samples were rinsed gently with PBS twice, fixed with 4% paraformaldehyde, stained by the Gram stain kit (BKMAN, China), and observed by optical microscopy (BX53M, Olympus, Japan). During the test for bacterial adhesion, a part of the partial P-TL and Ar-5 samples with bacteria were rinsed with the PBS buffer using a parallel-placed syringe. The zeta potential was measured on the Zetasizer Nano ZS (Malvern, UK) after ultrasonically collecting the attached bacteria from the samples. To analyze the other interaction factors, molecular dynamic simulation was performed on the simulated bacterial membrane composed of a mixture of palmitoyloleoyl-phosphatidylethanolamine and palmitoyloleoylphosphatidylglycerol (3:1 ratio) and PEEK nanoplates as the models. The martini coarse grain force field, one of the commonly used and extensively validated force field and periodic boundary conditions, was adopted in the computation [1]. The PEEK nanoplates with different orientations (θ = 90°or 30°) were put under the simulated bacterial membrane and a time duration of 60 ns with a coupling constant of 2 fs was applied to the isothermal-isochoric ensemble. In the simulation, the temperature was maintained at 298.15 K by the Berendsen method with the coupling constant of 1.0 ps [2]. In each run, the SHAKE algorithm and particle mesh Ewald method were used to determine the bond lengths and long-range electrostatic interactions, respectively. A 20 Å cut-off was used for the van der Waals forces and Coulomb interactions and the simulation was performed using the Groningen MAchine for Chemical Simulation (GROMACS)[3]. The generated trajectories were evaluated by the GROMACS inbuilt tools and the results were visualized using visual molecular dynamics [4].

In vitro cell culture

The osteoblasts (MC3T3-E1 cells) obtained from ATCC were cultured with Dulbecco's modified eagle medium (DMEM, Hyclone, USA) containing 10% fetal bovine serum (FBS, Gibco, USA) in an incubator at 37 ˚C under 5% CO_2, and 90% moisture. Before the experiments, the cells were detached from the culture dishes, centrifuged (1200 rpm, 5 min), and diluted to about 2×10^4 cells mL^{-1} with the fresh medium. In osteogenic induction, the

culture medium was supplemented with 50 μg/ml ascorbic acid, 10 mM β-glycerophosphate and 100 nM dexamethasone.

Cell viability and morphology

1 mL of the cell suspension (2×10^4 cells mL^{-1}) were added to each sample on the 24-well plate and incubated for 1, 3 and 7 days. At each time point, the culture medium was replaced with DMEM containing 10% 3-(4,5-dimethylthiazol-2-yl)-2,5-diphenyltetrazolium bromide and incubated for another 4 hours for formazan formation. Subsequently, the formazan product was dissolved by dimethyl sulfoxide and the absorbance at 570 nm was measured. Cell apoptosis/necrosis was analyzed by using the Annexin V-FITC/PI assay kit (Beyotime, China) and a flow cytometer (CytoFLEX, Beckman Coulter, USA). Briefly, 1 mL of the cell suspension with a density of 5×10^4 cells mL^{-1} was added to each sample and incubated for 1 and 3 days, respectively. Afterwards, the cells on each sample were harvested and stained with FITC and PI following the manufacturer's instructions, and finally analyzed by flow cytometry. Before examining the cell morphology by SEM (SEM, XL30 FEG, Philips, Netherlands), the cells were cultured for 1 day, rinsed twice with PBS, immobilized with 4% glutaraldehyde solution, dehydrated with gradient ethanol, dried at 37 ˚C and sputtered with platinum.

Alkaline phosphatase (ALP) assay and alizarin red staining

After osteogenic induction for 7 and 14 days, the cells in the different groups were treated with the cell lysis buffer (Beyotime, China) and the ALP activity and total intracellular protein were determined using the ALP Assay Kit (Beyotime, China) and BCA Protein Assay Kit (Beyotime, China), respectively. The ALP activity was normalized to the total protein content and quantitatively presented as nmol/min/mg protein. The degree of mineralization was evaluated by alizarin red staining. After osteogenic induction of osteoblasts on different samples for 14 days, the attached cells were washed three times with PBS, fixed in 75% ethanol for 1 hour, and stained with 1% alizarin red solution (pH 4.2, Solarbio, China) for 10 min. Afterwards, the unbound dye was removed by flushing with water and the stained samples were observed using a stereoscopic microscope (Stemi SV11, Zeiss, Germany). In the semi-quantitative analysis, the bound stain was eluted with 10% acetic acid and the absorbance at 405 nm was monitored by a microplate reader (Multimode microplate reader, Bio Tek, USA).

Quantitative real-time polymerase chain reaction (qPCR)

After osteogenic induction for 14 and 21 days, the total RNA was extracted from the cells in different groups by adding Trizol reagent (Invitrogen, USA). The complementary DNA (cDNA) was synthesized from 1000 ng of total RNA using a PrimeScript RT Master Mix kit (TaKaRa, Japan) following the manufacturer's instructions. The expressions of osteogenic

genes including ALP, osteocalcin (OCN), and osteopontin (OPN) were quantitatively analyzed by performing qPCR on a CFX96 detection system (BioRad, USA) using a mixture of TransStart Green qPCR SuperMix UDG Kit (TransGen Biotech, China). β-actin was selected as the housekeeping gene and the $2^{-\Delta\Delta Ct}$ method was employed to calculate the relative gene expression levels. The target genes (ALP, OCN, OPN and β-actin) and corresponding primer sequences are listed in Table S1.

Co-culture of bacteria and osteoblasts

For co-culturing bacteria and osteoblasts on different samples, 100 μL of the bacterial suspension (10^5 CFU mL^{-1}) was initially added to each sample on the 24-well plate and cultured for 3 hours. Afterwards, each sample was rinsed twice with PBS, and then 1 mL of the cell suspension (2×10^4 cells mL^{-1}) was added. After 1 day of co-culture, each sample was rinsed twice with PBS, immobilized with 4% glutaraldehyde solution, dehydrated with gradient ethanol, dried at 37 ˚C, sputtered with platinum and observed by SEM (Phenom Pro G6, Thermo Scientific, China). After 1 and 3 days of co-culture, each sample was rinsed twice with PBS, immobilized with 4% glutaraldehyde solution, stained for the cell nuclei with 5 μg/mL Hoechst 33342 (Yeasen Biotechnology, Shanghai, China) and examined by fluorescent microscopy (BX53, Olympus, Japan).

In vivo experiments

The animal experiments were approved by the Ethics Committee for Animal Research of Shenzhen Institutes of Advanced Technology, Chinese Academy of Sciences. 12-week-old male Sprague Dawley (SD) rats with weight of 250-300 g were maintained under specific pathogen free conditions and used in the following *in vivo* experiments for 6 rats in each group. To evaluate the anti-infective performance *in vivo*, 100 μL of the *E. coli* solution (10^6 CFU mL^{-1}) were seeded onto the samples (pristine PEEK, P-VL and P-TL) with dimensions of Φ10 × 1 mm and cultured for 1 hour. Afterwards, the contaminated samples were subcutaneously implanted into the two backsides of the depilated rats and the incisions were carefully closed. After 7 days, the rats were sacrificed and the specimens were harvested and H&E staining was performed to evaluate the inflammatory response of the peri-implant tissues. In the osteogenesis assessment, a horizontal defect (2 mm in diameter) was drilled in the tibia in the back-legs of each rat and the implants were inserted into the openings. The experimental rats were sacrificed after 8 weeks and the femurs containing the implants were harvested and fixed in paraformaldehyde. The peri-implant newly formed bone was imaged by micro-CT (SkyScan 1176, Bruker, Germany) and the 3D images were reconstructed using the NRecon software (Skyscan) and CTvol program (SkyScan). A hollow cylinder with a thickness of 50 μm from

the implant surface and length of 6 mm of the implant was defined as the volume of interest. Qualitative analyses of bone volume/total volume (BV/TV) and trabecular number (Tb.N) are more substantial on P-TL with a relatively low trabecular separation (Tb.Sp) conducted by 3D bone morphometric analysis. The fixed tissue and implant were decalcified in ethylenediaminetetraacetic acid for 1 month and embedded in paraffin to prepare the bone tissue sections. Finally, the thin sections were stained with Van Gieson and hematoxylin and eosin (H&E) to assess peri-implant bone regeneration. To observe the bone-implant interfaces, Van Gieson staining was carried out on the longitudinal slices prepared from the un-decalcified samples.

Statistical analysis

The experiments were performed at least in triplicate. The data were analyzed by the one-way ANOVA and shown as mean ± stand deviation (SD). A difference of $^{*}p < 0.05$ was considered to be significant and that of $^{**}p < 0.01$ or $^{***}p < 0.001$ was considered to be highly significant.

References

1 S. J. Marrink, H. J. Risselada, S. Yefimov, D. P. Tieleman and A. H. de Vries, *J. Phys. Chem. B*, 2007, **111**, 7812–7824.

2 H. J. C. Berendsen, J. P. M. Postma, W. F. van Gunsteren, A. DiNola and J. R. Haak, *J. Chem. Phys.*, 1984, **81**, 3684–3690.

3 M. J. Abraham, T. Murtola, R. Schulz, S. Páll, J. C. Smith, B. Hess and E. Lindahl, *SoftwareX*, 2015, **1–2**, 19–25.

4 W. Humphrey, A. Dalke and K. Schulten, *J. Mol. Graph.*, 1996, **14**, 33–38.

B. Supplementary Figures

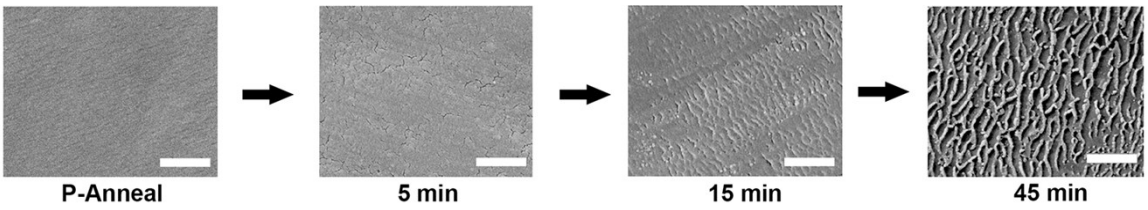

Fig. S1. Formation of the nanolamellar structure on the annealed PEEK as the argon plasma treatment is increased (scale bar = 500 nm).

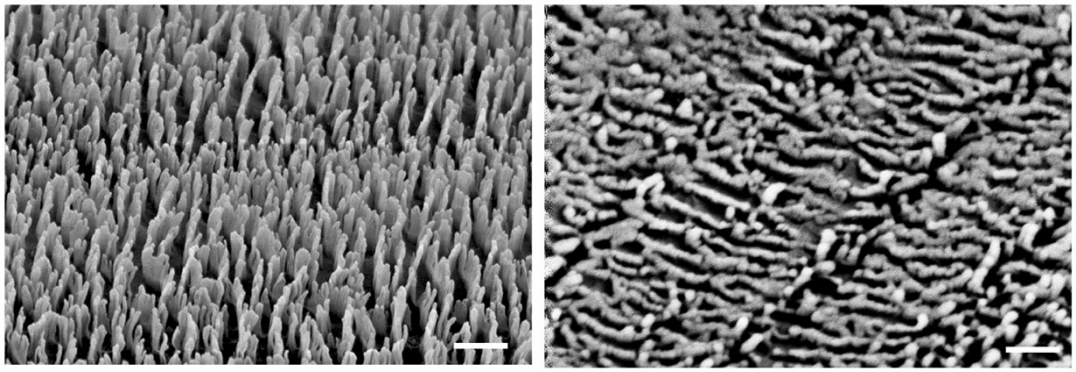

Fig. S2. The SEM images of PV-L and PT-L observed from side view at an angle of 45° (scale bar = 200 nm).

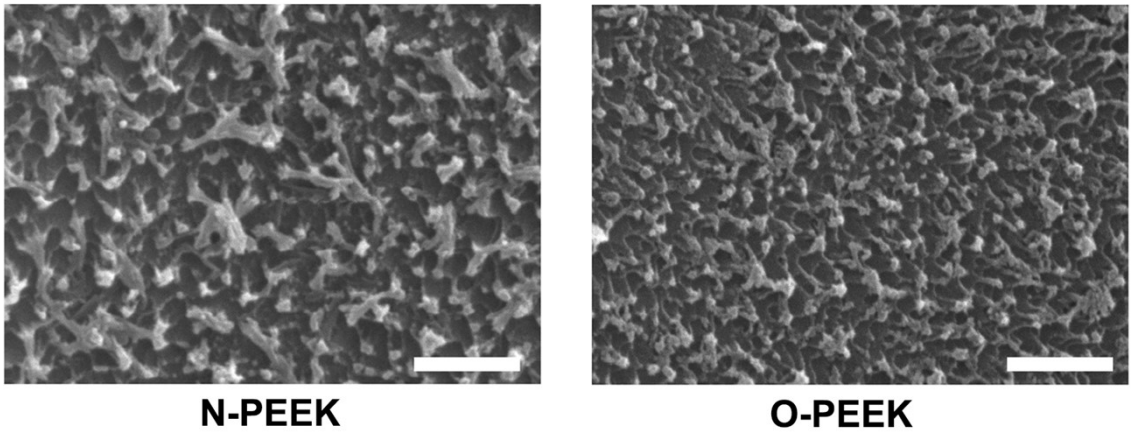

Fig. S3. SEM images of the nano-morphology on PEEK after treatment with the nitrogen plasma (N-PEEK) and oxygen plasma (O-PEEK) using the same parameters as the Ar plasma treatment (scale bar = 500 nm).

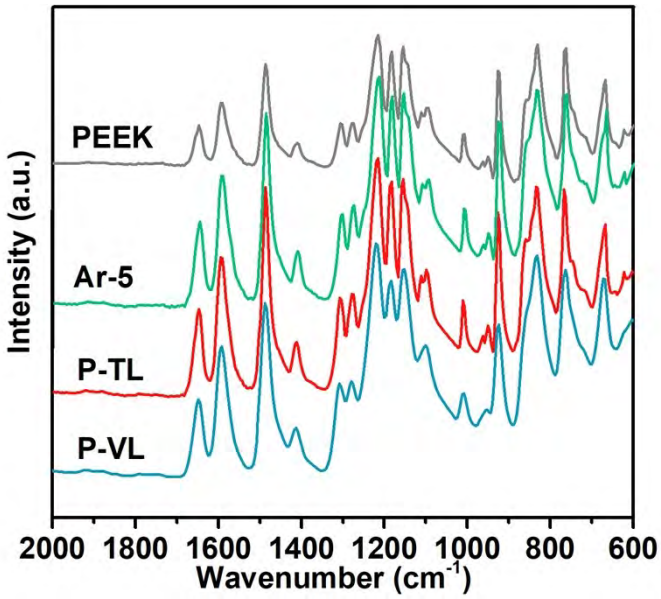

Fig. S4. ATR-FTIR spectra acquired from the different samples showing the absence of new functional groups after the Ar plasma treatment.

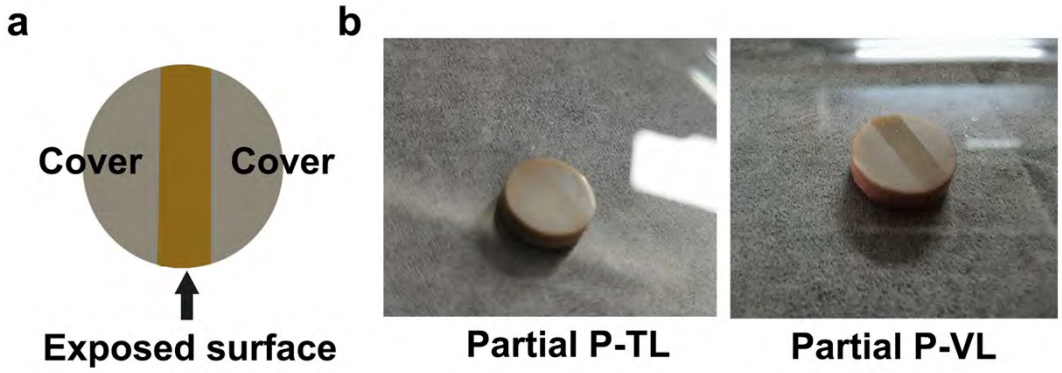

Fig. S5. (a) Illustration of the preparation of the partial P-TL and partial P-VL samples: Two regions of the substrates are shielded by silicon wafers and a middle region is exposed to the Ar plasma. (b) Pictures of the partial P-TL and partial P-VL samples showing different reflections from the middle regions.

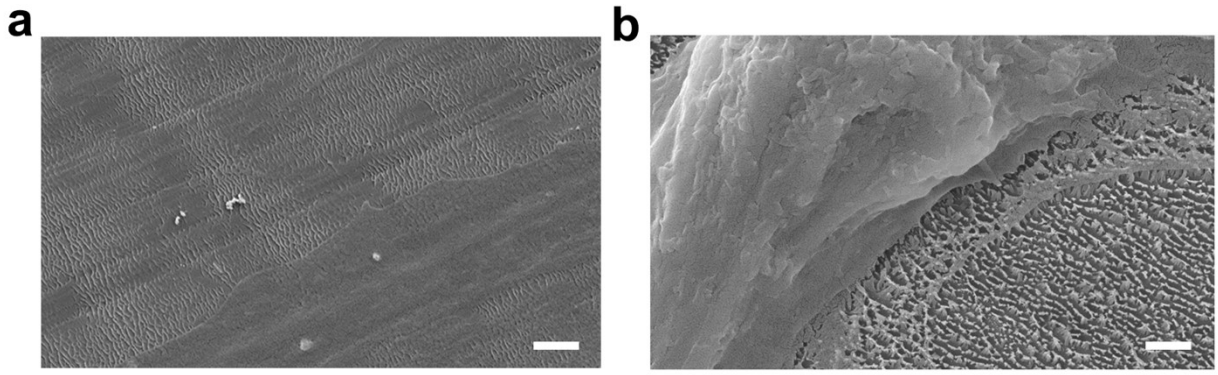

Fig. S6. SEM images showing the behavior of osteoblasts on (a) P-TL and (b) P-VL (scale bar = 1 μm).

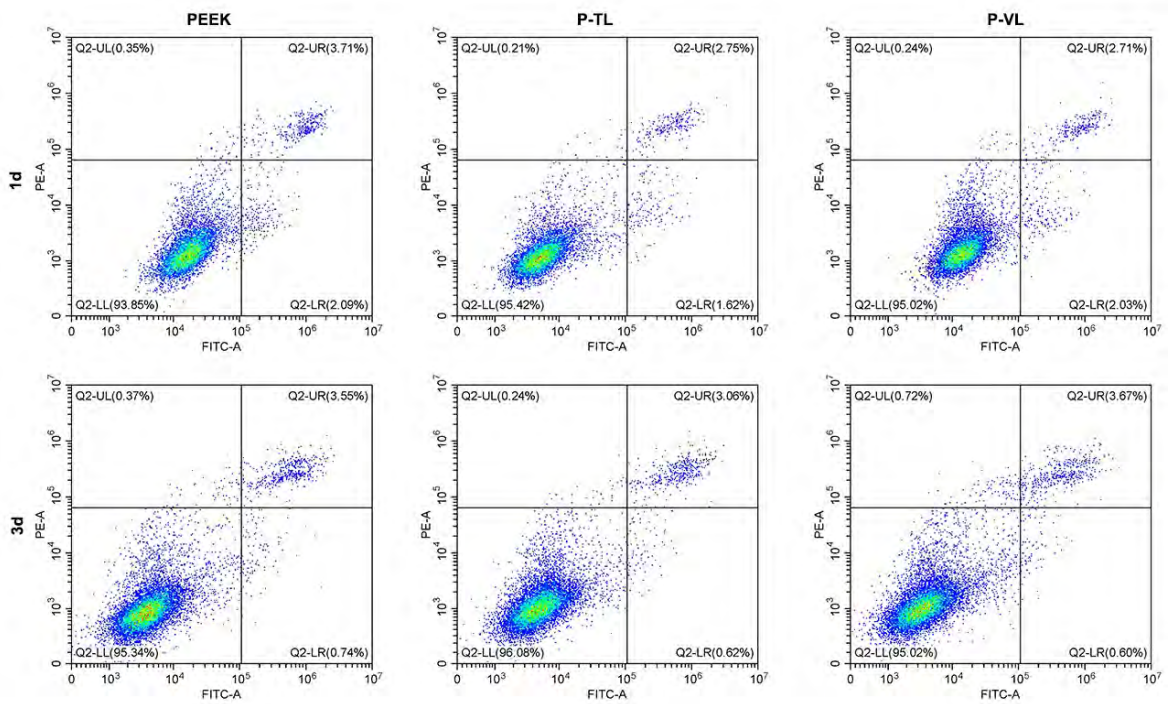

Fig. S7. Flow cytometry analysis (cell apoptosis and necrosis) of osteoblasts cultured on different samples for 1 and 3 days.

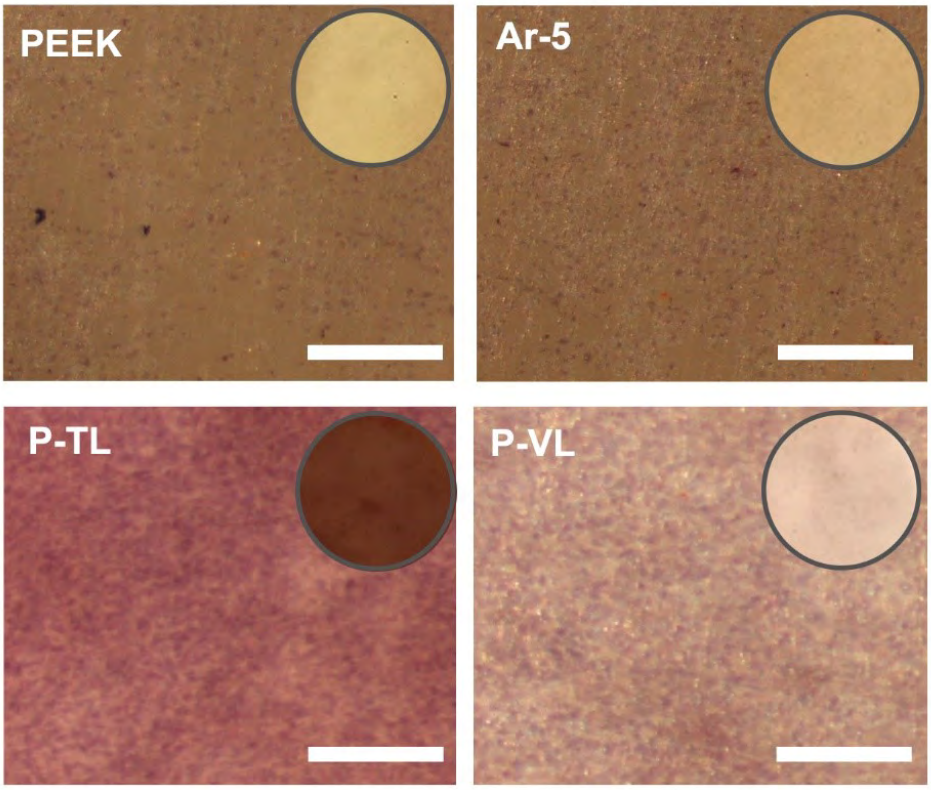

Fig. S8. Images showing mineralization of osteoblasts on the different samples after osteogenic induction for 14 days with the large-area images shown in the insets on the top-right (scale bar = 500 μm).

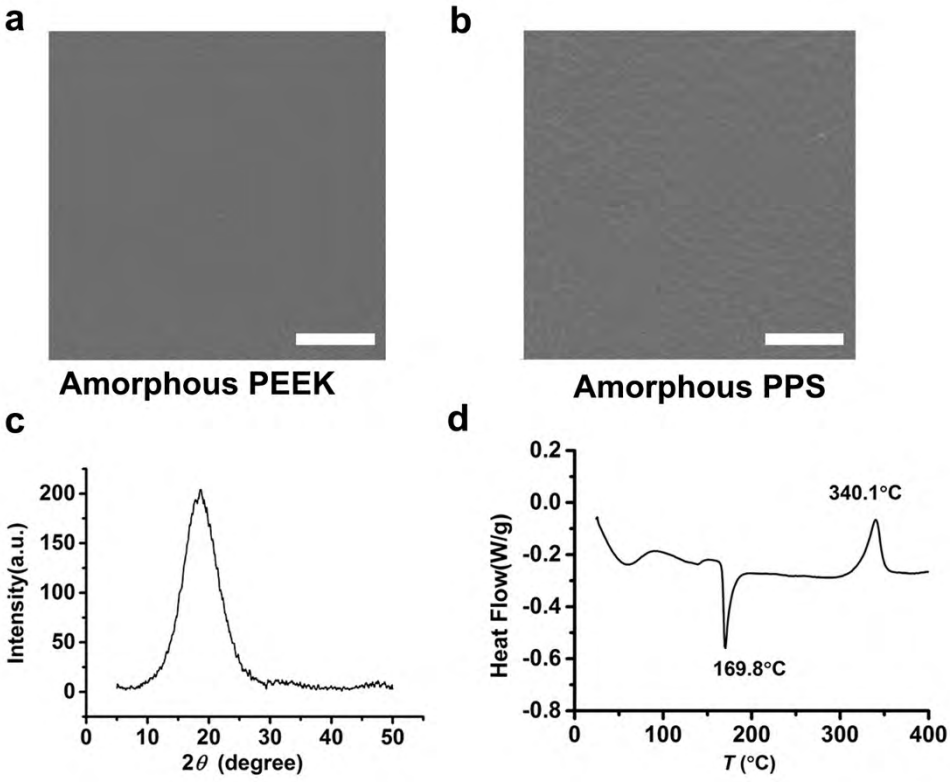

Fig. S9. SEM images of (a) Amorphous PEEK, (b) PPS after the Ar plasma treatment (scale bar = 500 nm); (c) XRD spectrum of PEEK; (d) DSC curve of PPS.

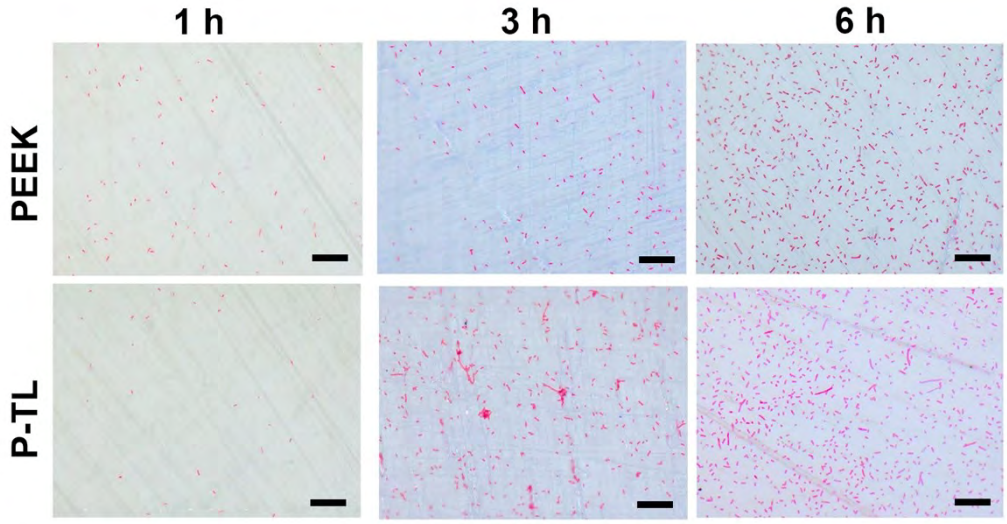

Fig. S10. Gram staining images of *E. coli* on PEEK and P-TL after incubation for 1, 3 and 6 hours (scale bar = 20 μm).

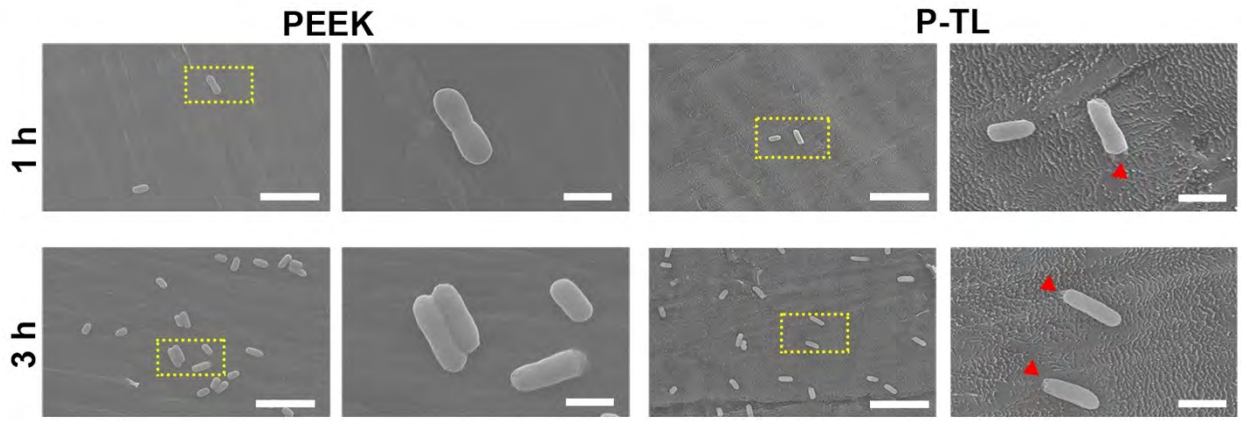

Fig. S11. SEM images of *E. coli* on PEEK and P-TL after incubation for 1 and 3 hours with the red triangles indicating defects at the poles of the cultured bacteria due to the initial destructive effect [scale bar (left column) = 5 μm; scale bar (right column) = 1 μm].

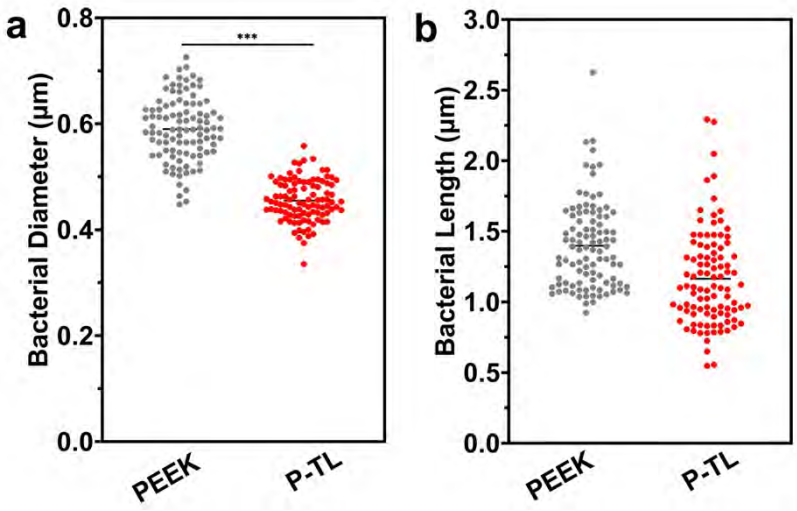

Fig. S12. (a) Diameters and (b) Lengths of *E. coli* on PEEK and P-TL after incubation for 3 hours with the bacteria size measured by ImageJ software. *** $p < 0.001$ was considered to be highly significant.

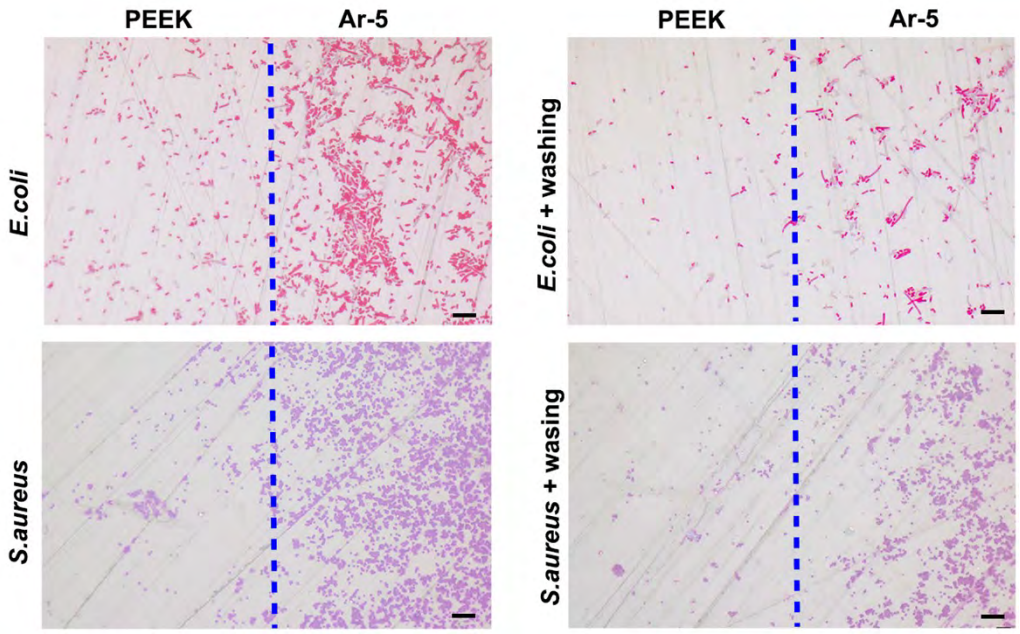

Fig. S13. Gram staining images of *E. coli* and *S. aure*us attached to the partial Ar-5 samples before and after PBS washing (scale bar = 10 μm). The blue line represents the boundary between the PEEK regions (left) and Ar-5 regions (right).

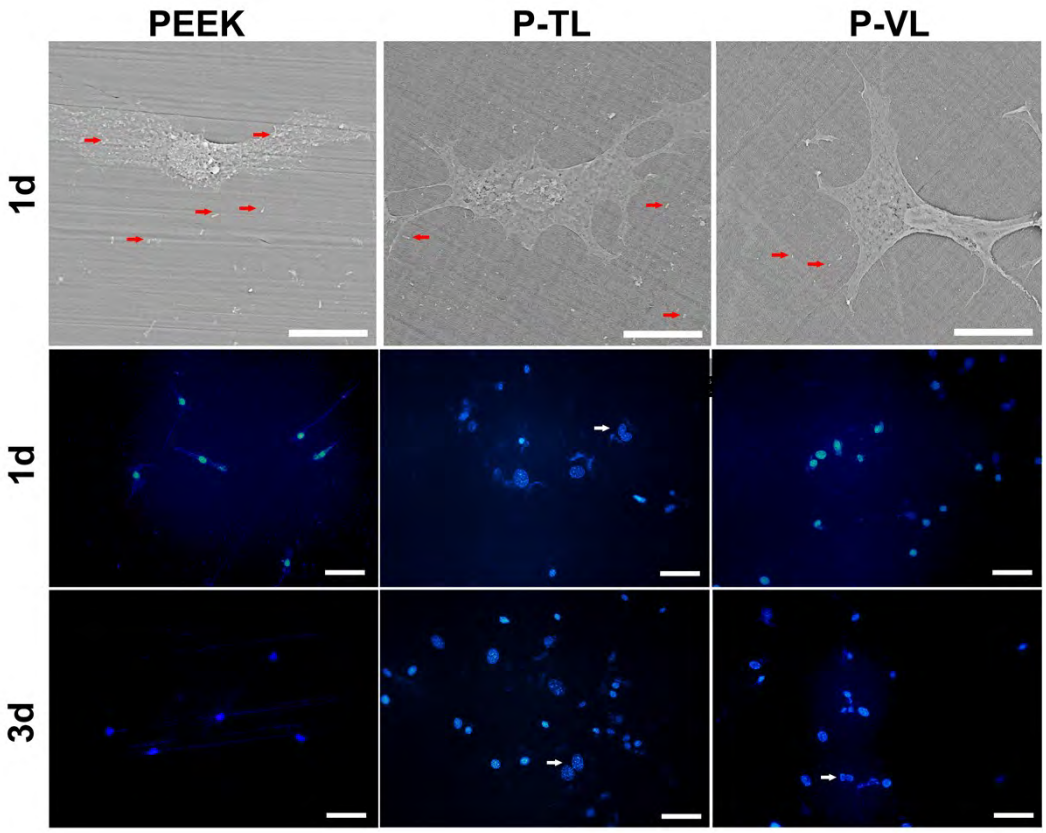

Fig. S14. (a) SEM images of bacteria and osteoblasts co-cultured on different samples for 1 day, red arrows indicate the presence of bacteria (scale bar = 20 μm). (b) Fluorescent staining images of bacteria and osteoblasts co-cultured on different samples for 1 and 3 days, white arrows indicate the growth and division of osteoblasts (scale bar = 50 μm).

Table S1. Primer sequences for the qPCR analysis.

Primers	Sequences (5’-3’)
β-actin	Forward: CGTAAAGACCTCTATGCCAACA Reverse: AGCCACCAATCCACACAGAG
ALP	Forward: TCAGAAGCTAACACCAACG Reverse: TTGTACGTCTTGGAGAGGGC
OCN	Forward: GCAAAGGTGCAGCCTTTGTG Reverse: GGCTCCCAGCCATTGATACAG
OPN	Forward: TCACCTGTGCCATACCAGTTAA Reverse: GGCTCCCAGCCATTGATACAG